Accepted Manuscript

Construction of $NiCo_2O_4@MnO_2$ nanosheet arrays for high-performance supercapacitor: Highly cross-linked porous heterostructure and worthy electrochemical double-layer capacitance contribution

Li Su, Lijun Gao, Qinghua Du, Liyin Hou, Zhipeng Ma, Xiujuan Qin, Guangjie Shao

PII: S0925-8388(18)31230-1

DOI: 10.1016/j.jallcom.2018.03.353

Reference: JALCOM 45583

To appear in: *Journal of Alloys and Compounds*

Received Date: 11 January 2018

Revised Date: 25 March 2018

Accepted Date: 27 March 2018

Please cite this article as: L. Su, L. Gao, Q. Du, L. Hou, Z. Ma, X. Qin, G. Shao, Construction of $NiCo_2O_4@MnO_2$ nanosheet arrays for high-performance supercapacitor: Highly cross-linked porous heterostructure and worthy electrochemical double-layer capacitance contribution, *Journal of Alloys and Compounds* (2018), doi: 10.1016/j.jallcom.2018.03.353.

Construction of $NiCo_2O_4$@MnO_2 nanosheet arrays for high-performance supercapacitor: Highly cross-linked porous heterostructure and worthy electrochemical double-layer capacitance contribution

Li Su[†,‡], Lijun Gao[‡], Qinghua Du[‡], Liyin Hou[‡], Zhipeng Ma[‡], Xiujuan Qin[**,†,‡], Guangjie Shao[*,†,‡]

† State Key Laboratory of Metastable Materials Science and Technology, Yanshan University, Qinhuangdao 066004, China

‡ Hebei Key Laboratory of Applied Chemistry, College of Environmental and Chemical Engineering, Yanshan University, Qinhuangdao 066004, China

*Corresponding author at: College of Environmental and Chemical Engineering, Yanshan University, Qinhuangdao 066004, China

**Corresponding author at: College of Environmental and Chemical Engineering, Yanshan University, Qinhuangdao 066004, China

E-mail address: shaoguangjie@ysu.edu.cn (G. Shao), qinxj@ysu.edu.cn (X. Qin)

Tel.: 0086-335-8061569; Fax: 0086-335-8059878.

Abstract: A highly cross-linked three-dimensional (3D) hierarchical porous $NiCo_2O_4$ nanosheet@MnO_2 nanosheet arrays (NNAs) on Ni foam is fabricated by a facile and stepwise hydrothermal approach. The $NiCo_2O_4$@MnO_2 hybrid electrode demonstrates excellent electrochemical properties with high area capacitance of 5.3 F cm^{-2} at 1 mA cm^{-2}, tremendous rate performance (68.9% with current density increased to 20 mA cm^{-2}), and outstanding cycling stability (90.1% capacitance retention over 5000 cycles at 20 mA cm^{-2}). The intriguing performance is related to unique cross-linked porous heterostructure with open geometry that provides large surface areas and superb channels for the electrolyte penetration and ion diffusion. Besides, by analyzing non-faradaic capacitive current upon repeated potential cycling, this honor attributes to not only sufficient Faraday reactions, but also a worthy electrochemical double-layer capacitance (EDLC) contribution with an electrochemical surface area (ESA) value of 616 mF cm^{-2} (220 F g^{-1} with a mass loading of 2.8 mg cm^{-2}), which approximates to that of porous carbon.

Keywords: $NiCo_2O_4$@MnO_2 NNAs; Cross-linked; EDLC contribution; Supercapacitors.

1. Introduction

With the fast energy crisis, extensive research efforts have been taken to explore for renewable, conversion and sustainable energy storage devices[1-10]. Supercapacitors, also known as electrochemical capacitors, have caused the extensive concern owing to their fast energy storage, high power density (>10 kW kg^{-1}), long lifespan, and environmental friendly, which remedy the lithium-ion batteries (LIBs) and fuel cells to some degree[11-14]. Currently, considerable research efforts mainly focus on the rational design of electrode materials with high electrochemical conductivity, large specific surface area and excellent electrochemical capacitance[15-18]. Various materials, including carbon materials for EDLC[19-21], transition metal oxides or sulfides[22-29], and conducting polymers for pseudocapacitor[30-32] have been widely studied as the electrode materials. Up to now, so many works have been focus on building composite materials of transition metal oxides and carbon materials, which attributes to the high theoretical capacitance of transition metal oxides and excellent electrical conductivity of various carbon materials[33, 34]. Nevertheless, owing to poor capacitance from carbon materials and simply combination with reducing the utilization of the active material, they possess relatively lower capacitance than composite materials of transition metal oxides and transition metal oxides[35]. Thus, selecting two suitable transition metal oxides as electrode material and constructing a proper electrode structure with large specific surface area and hierarchical porous act as EDLC capacitance contribution are especially significative for high-performance supercapacitor.

Up to now, $NiCo_2O_4$ has drawn much attention owing to its relatively well electrical conductivity, fast ion diffusion rate, and richer redox sites compared with binary oxides (NiO, Co_3O_4, etc.)[4, 36-39]. Also, MnO_2 has shown promise as advanced electrode due to its relatively high theoretical specific capacitance of 1370 F g^{-1} (as the oxidation state of Mn ion changes from +4 to +3 over a potential window of 0.8 V), earth-abundance and environmental friendliness[40-42]. Nevertheless, the

$NiCo_2O_4$ suffers from inferior capacitance retention and rate capability, while MnO_2 with poor conductivity (10^{-5}–10^{-6} S cm^{-1}) makes structural collapse during charge-discharge process, which greatly hinder their practical application[43, 44]. To address these problems, the immediate challenge motivated us to design a smart heterostructure with $NiCo_2O_4$ and MnO_2 materials to enhance the electrochemical performance through synergistic effects between the two components with different dimensions[45-47]. For core-shell nanostructure arrays, they possess large specific surface area with more active sites for loading additional active materials. Besides, cross-linked heterostructure with strong mechanics would avoid MnO_2 structural collapse during charge-discharge process. For example, Lou et al.[48] synthesized $NiCo_2O_4$@MnO_2 nanowire arrays, when the current density was 20 mA cm^{-2}, the capacitance could attain 1.66 F cm^{-2}, with a capacitance fading of 12% after 2000 cycles. Ma et al.[49] reported a hierarchical α-MnO_2 nanowires@$NiCo_2O_4$ nanoflakes core-shell nanostructure presented an improved capacitance of 1101 F g^{-1} at 1 A g^{-1} for pseudocapacitor with respect to that of pristine MnO_2 nanowire arrays. However, to the best of our knowledge, most of the previous researches on the $NiCo_2O_4$ and MnO_2 composites are still focused on nanowire arrays, and the hierarchical nanosheet arrays with widely open and cross-linking structures are rarely explored. As a scaffold for supporting MnO_2, the nanosheet arrays possess larger specific surface areas than nanowire arrays, and more active sites are exposed in electrolyte which contributing to fast ion diffusion and high EDLC contribution to some extent.

Herein, we present a rational fabrication of 3D cross-linked porous

$NiCo_2O_4@MnO_2$ nanosheet arrays with Ni foam as the substrate via a multi-step hydrothermal method combined with a post annealing treatment in air. Satisfactorily, this smart electrode design offers several advantages as follows: First, as a binder-free electrode with 3D network structure, it can provide fast electron pathway and avoid nonsensical adhesive. Second, $NiCo_2O_4$ NAs with excellent electrochemical conductivity can be utilized as an ideal scaffold for loading additional active materials in view of their large surface area and avoid MnO_2 structural collapse during charge-discharge process. Third, ultrathin mesoporous MnO_2 nanosheets are coated on the surface of $NiCo_2O_4$ nanosheets, which leads to a highly interconnected network structure with rich porosity and promotes electrochemical reaction. Fourth, owing to the enlarged active surface area of the hierarchical structure, $NiCo_2O_4@MnO_2$ NNAs possess a high EDLC contribution with an ESA value of 616 mF cm^{-2}. In a word, this unique 3D hybrid nanostructure can enable the full utilization of both core and shell materials, and offer superb channels for the electron transport and ion diffusion. The high area specific capacitance combines the faradaic capacitance from redox reactions and the EDLC on the surface of the hierarchical structure, which benefits for realizing practical applications. Moreover, the morphologies of $NiCo_2O_4@MnO_2$ with different reaction time are discussed in detail to find the most appropriate candidate for energy storage.

2. Experimental section

2.1. Synthesis of $NiCo_2O_4$ NAs on Ni foam

The $NiCo_2O_4$ NAs was synthesized by using a hydrothermal method. First of all, the ready Ni foam was slightly disposed with ethanol and deionized water to remove the surface impurities. Next, 1 mmol $Ni(NO_3)_2 \cdot 6H_2O$, 2 mmol $Co(NO_3)_2 \cdot 6H_2O$, 6 mmol NH_4F, and appropriate urea were dissolved into 80 mL deionized water and stirred ceaselessly to become homogeneous solution. Then, the solution was poured into a 100 mL Teflon autoclave and kept it at 120 °C for 3h. Waiting for the stainless steel autoclave cooled down, the Ni foam coated as-prepared sample was collected from the solution and then washed with deionized water and absolute ethanol several times to remove residual impurity. Finally, the coated was calcinated at 350 °C for 2 h in air, and the $NiCo_2O_4$ NAs grown on Ni foam substrate was obtained. The areal mass loading of $NiCo_2O_4$ NAs is 1.2 mg/cm^2.

2.2. Synthesis of $NiCo_2O_4$@MnO_2 NNAs

The as-prepared $NiCo_2O_4$ NAs on Ni foam was directly used as the scaffold to support the MnO_2 nanosheets via the second hydrothermal process. The Ni foam coated $NiCo_2O_4$ NAs was also put inside the Teflon-lined stainless steel autoclave with a 0.03 M $KMnO_4$ solution. Then keep it at a temperature of 160 °C for 5 h. The final as-synthesized materials were washed and dried to obtain the 3D $NiCo_2O_4$@MnO_2 NNAs on Ni foam substrate. The areal mass loading of $NiCo_2O_4$@MnO_2 NNAs is 2.8 mg/cm^2. Moreover, the appropriate content and morphology of MnO_2 were controlled by different reaction time (1h, 3h, 5h, 8h, and 12h).

2.3. Materials characterization

X-ray powder diffraction (XRD, RigakuSmart Lab, X-ray Diffractometer, Japan) was performed to study the crystalline structure of the products. In addition, nitrogen adsorption-desorption isotherms tested on a VSorb 2800P analyzer was used to evaluate the surface area and pore structure of the materials using Brunauer-Emmett-Teller (BET) method. The detailed morphology of the materials were characterized by field-emission scanning electron microscopy (FE-SEM, Carl Zeiss Super55 operated at 5 kV) and field-emission transmission electron microscope (TEM, Hitachi HT7700 operated at 120 kV), respectively.

2.4. Evaluations of electrochemical properties

The main electrochemical tests as follows. Electrochemical tests were carried out in three-electrode system and performed in a 6 M KOH aqueous solution, pure $NiCo_2O_4$ NAs or 3D $NiCo_2O_4$@MnO_2 NNAs on Ni foam was directly as the working electrode, active carbon (AC) as the counter electrode, and Hg/HgO electrode as the reference electrode, respectively. Galvanostatic charge−discharge testing system (NEWARE, Shenzhen, China) at different current density with a range of voltage window from -0.1 to 0.55 V vs Hg/HgO. The cyclic voltammetry (CV) and the electrochemical impedance spectroscopy (EIS) were performed on a CHI 660E electrochemical workstation. CV measurements were carried out from -0.1 to 0.55 V at the different scanning rates and EIS was measured within a frequency range of 0.01 to 100000 Hz. The area capacitance of electrode materials was estimated from the charge-discharge test according to the following equation:

$$Ca = I\,\Delta t / (S\Delta V) \qquad (1)$$

$$Cm = I\,\Delta t\,/\,(m\Delta V) \tag{2}$$

Where Ca is the area specific capacitance (F cm^{-2}), Cm (F g^{-1}) is the mass specific capacitance, I is the charge−discharge current (A), Δt is the discharge time (s), ΔV is the charge−discharge potential window (V), S is the geometrical area of the active material (cm^2), and m is the mass loading of the electrode (g).

3. Results and Discussions

In this work, the fabrication of hierarchical $NiCo_2O_4@MnO_2$ NNAs on Ni foam mainly involves two key steps, as illustrated in **Fig. 1**. In the first step, the Ni-Co

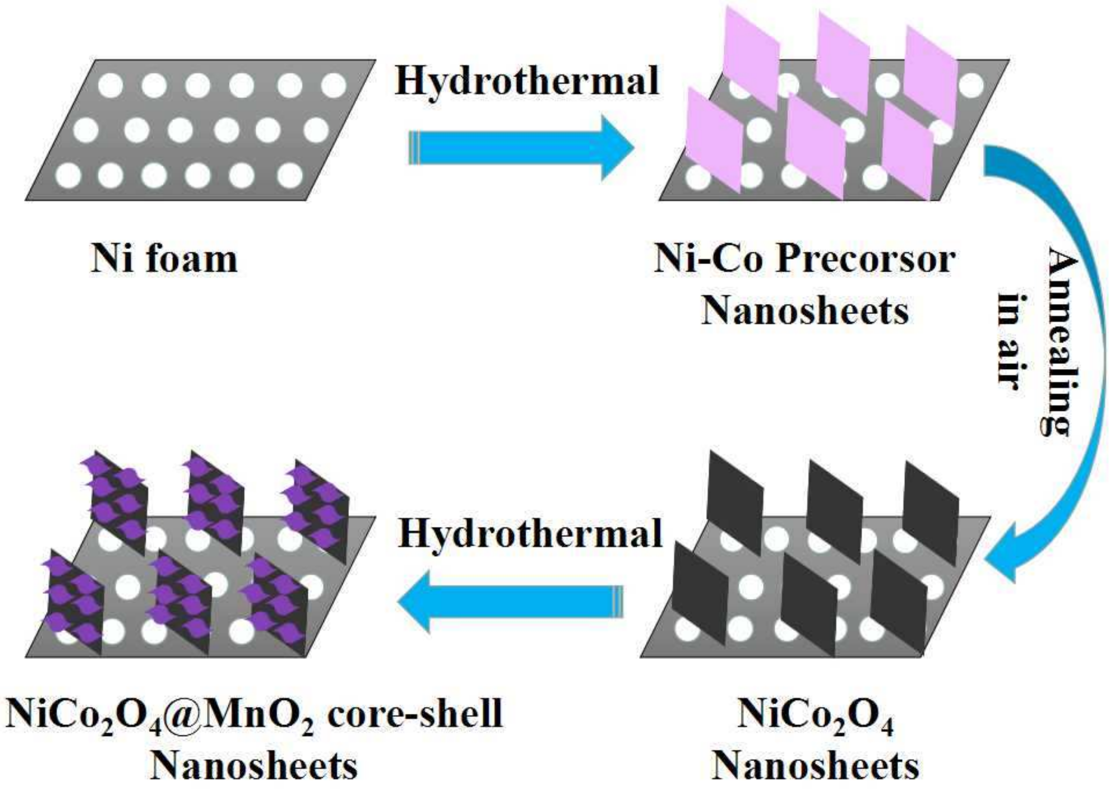

Fig. 1 Schematic illustration of the formation process of $NiCo_2O_4@MnO_2$ NNAs.

precursor nanosheet arrays were grown on the nickel foam by using a hydrothermal method. After the annealing treatment at 350°C for 2 h in the air, $NiCo_2O_4$ NAs are fully converted into a highly porous architecture. In the following step, ultrathin and mesoporous MnO_2 nanosheets were subsequently coated on the scaffold of $NiCo_2O_4$ via a facile hydrothermal method again, leading to the successful construction of hierarchical $NiCo_2O_4$@MnO_2 core-shell NNAs on Ni foam.

SEM and TEM studies are employed to investigate the morphology of the as-synthesized $NiCo_2O_4$ NAs and $NiCo_2O_4$@MnO_2 NNAs. **Fig. S1** exhibits the typical morphology of pristine $NiCo_2O_4$ NAs on Ni foam. Notably, these nanosheets are interconnected with each other to form the 3D ordered network. It can be seen that the $NiCo_2O_4$ nanosheets possess an average thickness of approximately 50 nm with

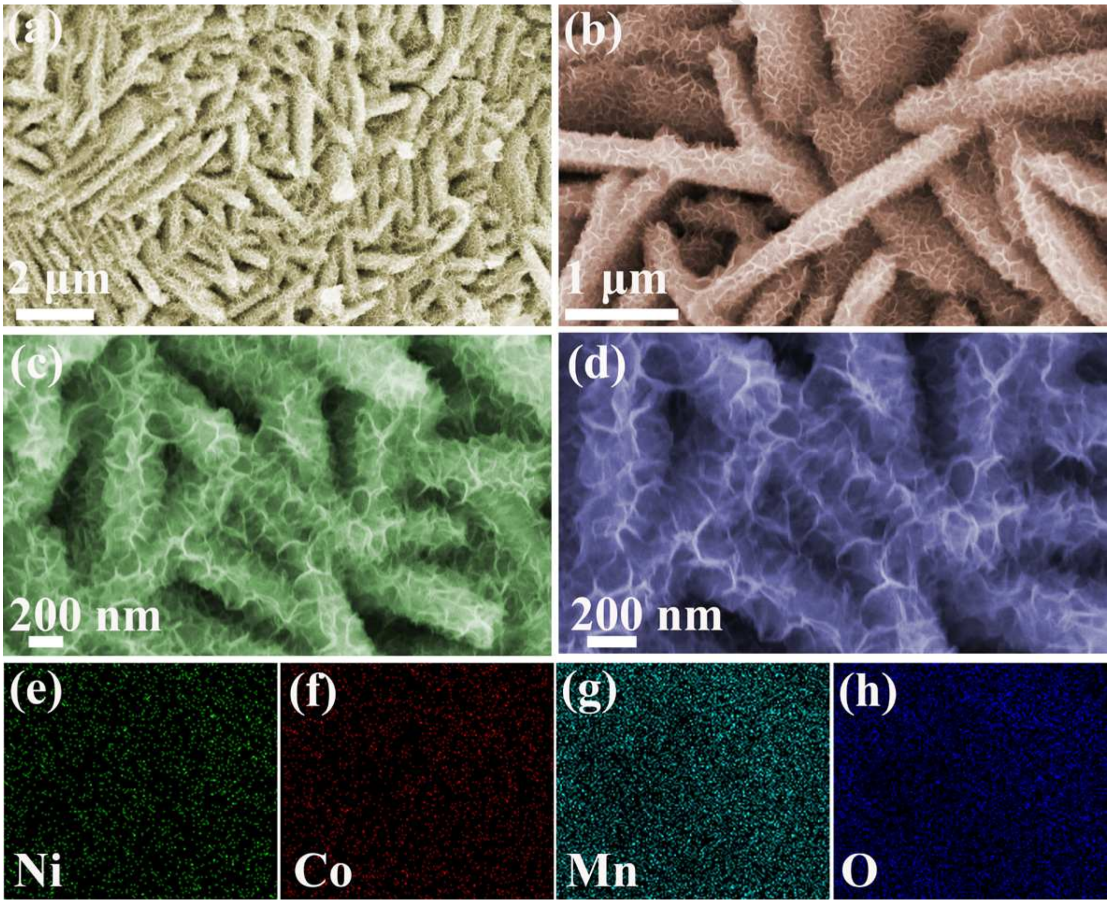

Fig. 2 Low and high-magnification FE-SEM images of (a, b, c, d) 3D $NiCo_2O_4$@MnO_2 NNAs; (e, f, g, h) Energy dispersive X-ray spectroscopy (EDS)

mapping image of $NiCo_2O_4$@MnO_2 NNAs.

dimension in the range of 2 to 3μm, which supports more additional active materials for further reaction. Besides, the energy dispersive X-ray spectroscopy (EDS) mapping presents a uniform distribution of element Ni, Co, and O within the $NiCo_2O_4$. After growing MnO_2 nanosheets, the morphology is shown in **Fig. 2**. It is worth noting that the whole surface of the $NiCo_2O_4$ scaffolds are obviously decorated with a few layers of thick MnO_2 nanosheet arrays, forming a dense core-shell hierarchical structure with large-scale, highly opened, and numerous accessible channels for electron transport. Furthermore, as shown in **Fig. 2d**, the thickness of hybrid material increases to 200 nm and the interconnected nanostructures are desired porous that benefit electrolyte penetration and ion diffusion for outstanding electrochemical performance. **Fig. 2e–h** shows the EDS mapping for $NiCo_2O_4$@MnO_2 NNAs, which presents a distribution of element Ni, Co, Mn, and O, indicating that MnO_2 exists in the material. Moreover, as can be seen in **Fig. S2a–2h**, the different morphology of $NiCo_2O_4$@MnO_2 core–shell nanostructure arrays have also been fabricated after hydrothermal process of growing the MnO_2 nanosheets at 160°C with other reaction time (1h, 3h, 8h, and 12h). When the hydrothermal reaction time of is just 1h (**Fig. S2a** and **S2e**) or 3h (**Fig. S2b** and **S2f**), the surface of $NiCo_2O_4$ NAs are nearly smooth owing to the insufficient reaction with a short time. However, as shown in **Fig. S2c** and **S2g** (with a reaction time of 8h), the surface of each $NiCo_2O_4$ nanosheet covers dense MnO_2 nanosheet arrays, and there are additional MnO_2 nanosheet clusters between $NiCo_2O_4$ nanosheets, which blocks some porous channels for electron and ion transport in electrolyte. Also showing in **Fig. S2d** and **S2h**, when the reaction time increases to 12h, a thick and uniform layer of MnO_2 nanoflakes are appeared, as well as no interconnected $NiCo_2O_4$ nanosheets exposed, indicating the mass decomposition of $KMnO_4$ as time goes on. Although it covers with uniform and porous MnO_2 ultrathin nanosheets, the hierarchical core-shell structure disappeared, and is not conducive to sufficient electrochemical reactions. To further reveal the microstructure of $NiCo_2O_4$@MnO_2 NNAs, the close-up TEM view (**Fig. 3a** and **3b**) indicates that an individual $NiCo_2O_4$ nanosheet is composed by nanocrystallites of 10 nm to form a highly porous structure. The SAED pattern of $NiCo_2O_4$ NAs (inset of **Fig. 3a**)

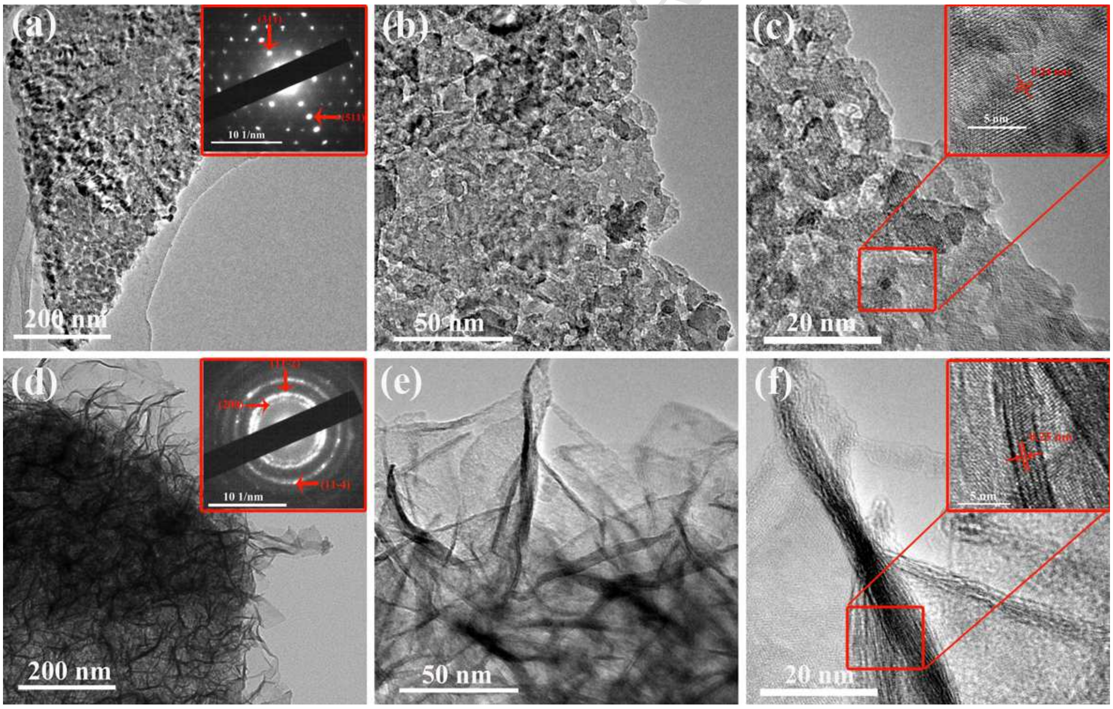

Fig. 3 (a, b) TEM images with different magnifications of $NiCo_2O_4$ NAs [inset of (a) is the corresponding SAED pattern of $NiCo_2O_4$ NAs]; (c) HR-TEM image of $NiCo_2O_4$ NAs [inset of (c) is the enlarged image of the $NiCo_2O_4$ NAs crystal lattice]; (d, e) TEM images with different magnifications of the 3D $NiCo_2O_4$@MnO_2 NNAs [inset

of (d) is the corresponding SAED pattern]; (f) HR-TEM image of the 3D $NiCo_2O_4$@MnO_2 NNAs [inset of (f) is an enlarged image of the MnO_2 nanosheet crystal lattice in the nanohybrid].

displays an orderly spot array, which are indexed to the (311) and (511) planes of $NiCo_2O_4$ crystal structure. The high resolution TEM (HRTEM) examination shown in **Fig. 3c** reveals a distinct set of visible lattice fringes with an inter-planar spacing of 0.24 nm, and it corresponds to the (311) plane of cubic $NiCo_2O_4$[50]. **Fig. 3d** displays the $NiCo_2O_4$@MnO_2 NNAs core-shell hierarchical structure, showing that ultrathin MnO_2 nanosheets interconnected with each other are uniformly grow on the surface of $NiCo_2O_4$ to form a wall-like structure. The SAED pattern of MnO_2 nanosheets (inset

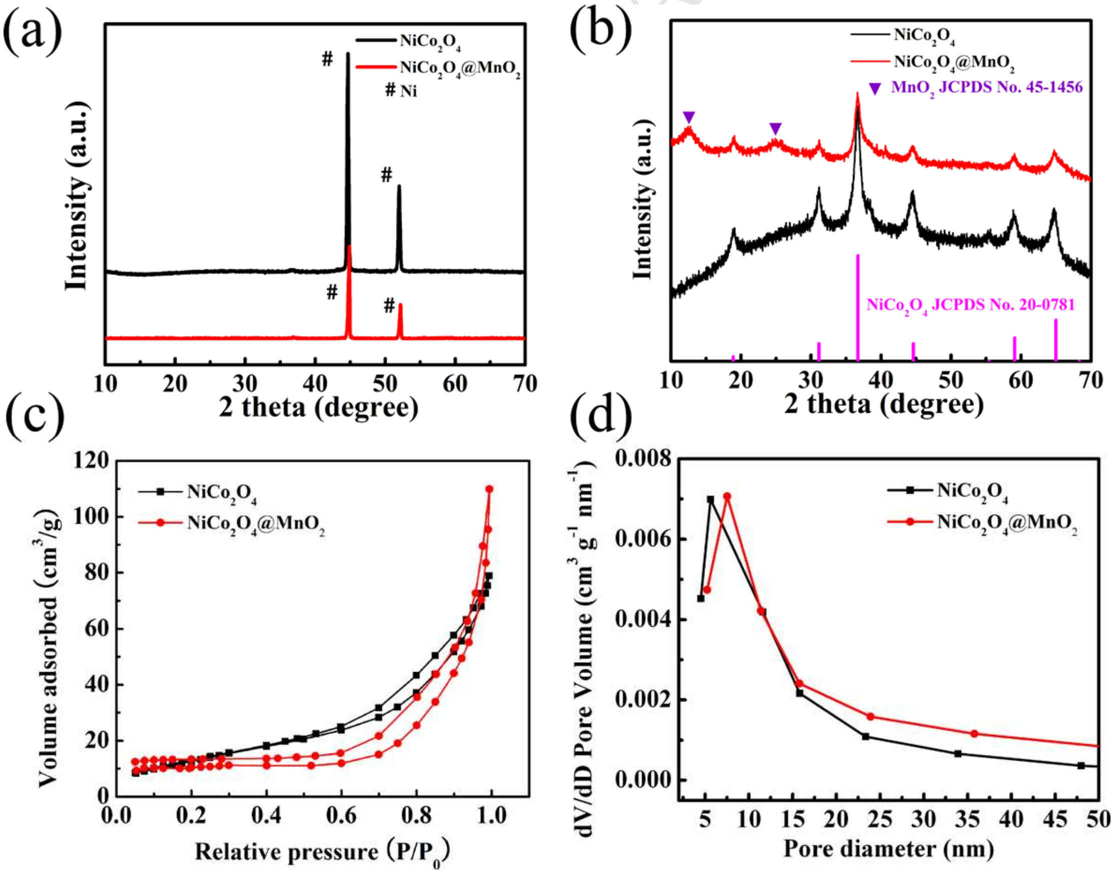

Fig. 4 XRD patterns of the (a)$NiCo_2O_4$ NAs and 3D $NiCo_2O_4$@MnO_2 NNAs on Ni foam; (b) $NiCo_2O_4$ NAs and 3D $NiCo_2O_4$@MnO_2 powder scratched from Ni foam; (c,

d) Nitrogen adsorptionedesorption isotherm and pore-size distribution curve of $NiCo_2O_4$ NAs and $NiCo_2O_4$@MnO_2 NNAs.

of **Fig. 3d**) presents three diffraction rings with polycrystal characteristic, which are indexed to the (200), (11-2) and (11-4) reflections of layered birnessite-type MnO_2 structure. That is also well demonstrated in the XRD analysis. As shown in **Fig. 3e**, MnO_2 nanosheets are ultrathin, and the HRTEM image (**Fig. 3f**) shows a noticeable interlayer spacing of 0.25 nm, which consistents with the (200) plane of layered birnessite-type MnO_2[51].

The crystal structure of the as-prepared products was investigated by XRD. **Fig. 4a** shows the XRD patterns of the $NiCo_2O_4$ NAs and $NiCo_2O_4$@MnO_2 NNAs on Ni foam. Owing to the thin film samples on the substrate, they both show the relatively weak peaks except for the obvious peaks of Ni. Furthermore, the distinct XRD patterns of $NiCo_2O_4$ and $NiCo_2O_4$@MnO_2 powder scratched from Ni foam are shown in **Fig. 4b**. Without the impact of Ni foam substrate, the clear diffraction peaks of samples are appeared. It can be seen from **Fig. 4b** that the $NiCo_2O_4$ NAs are well indexed as pure cubic phase $NiCo_2O_4$ (JCPDS card no. 20-0781) without any impurity peaks. In addition, the main peaks at 12.4° and 24.9° of birnessite-type MnO_2 (JCPDS card no. 43-1456) can be clearly identified from $NiCo_2O_4$@MnO_2 NNAs. BET analysis and BJH method were employed to verify the specific surface area and porous structure of hierarchical $NiCo_2O_4$@MnO_2 NNAs. For comparison, the nitrogen adsorption-desorption isotherm and pore-size distribution curve of both $NiCo_2O_4$ NAs and $NiCo_2O_4$@MnO_2 NNAs are present in **Fig. 4c** and **Fig. 4d**, respectively. It clearly indicates that both curves show a typical type IV isotherm with

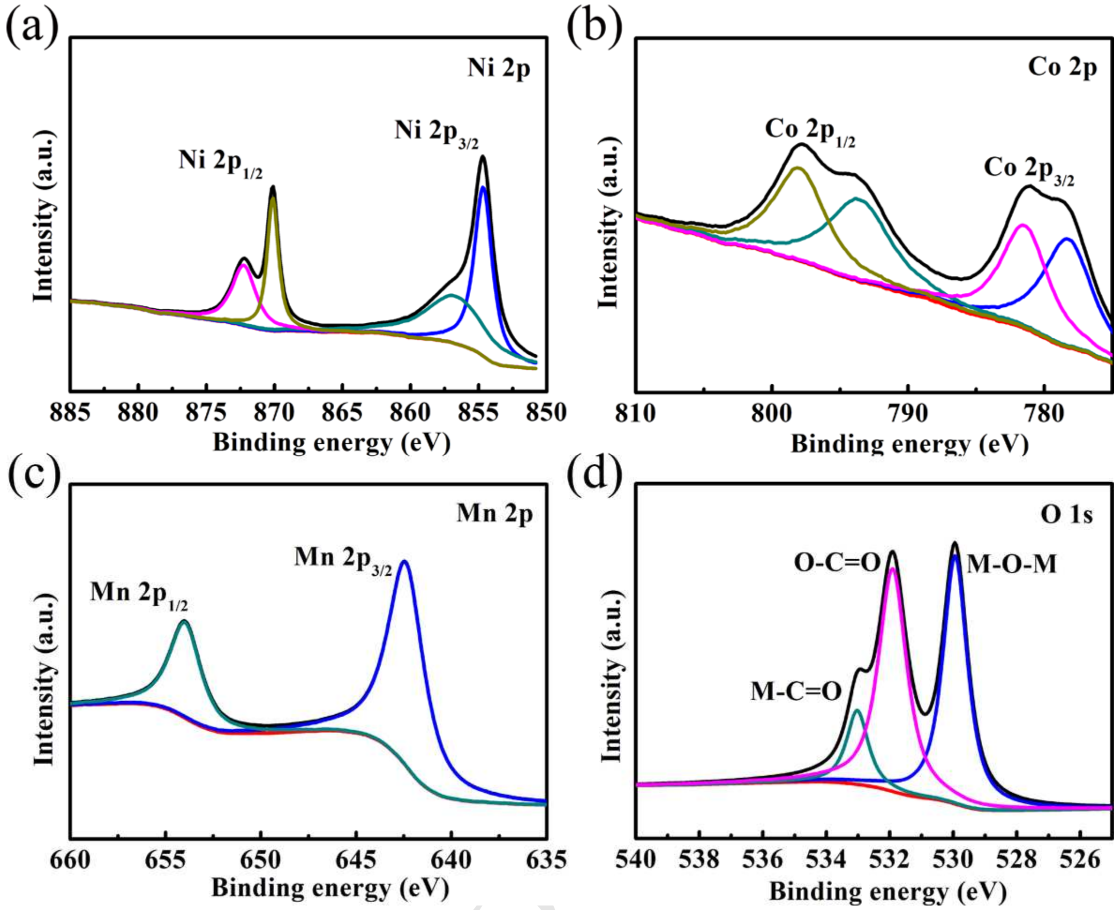

Fig. 5 XPS spectra of the (a) Ni 2p, (b) Co 2p, (c) Mn 2p, and (d) O 1s of $NiCo_2O_4$ @MnO_2 NNAs.

H3-type hysteresis loops ($P/P_0 > 0.4$), suggesting the mesoporous structures of the two samples. Besides, the $NiCo_2O_4$@MnO_2 NNAs reveals a high BET surface area of (50.02 m^2 g^{-1}), which is significantly higher than that of the $NiCo_2O_4$ NAs (33.44 m^2 g^{-1}). In addition, it can be clearly seen from **Fig. 4d** that the pore diameter distribution of the $NiCo_2O_4$@MnO_2 NNAs is superior to that of the $NiCo_2O_4$ NAs, which provides more spacious channels for ion imbedding and promotes energy storage. X-ray photoemission spectroscopy (XPS) results of the $NiCo_2O_4$@MnO_2 NNAs are also presented in **Fig. 5a–d**. In the XPS spectrum of the de-convoluted Ni 2p region (**Fig.**

5a), the binding energy situated at 854.6 eV and 870.1 eV in Ni $2p_{3/2}$ and Ni $2p_{1/2}$, respectively, corresponds to the characteristics of Ni^{2+}. And peaks at 856.2 eV in Ni $2p_{3/2}$ and 872.8 eV in Ni $2p_{1/2}$ are ascribed to Ni^{3+}. The de-convoluted Co 2p displays the electronic configuration of Co atoms as shown in **Fig. 5b**, where the fitting peaks at 778.3 and 793.6 eV are indexed to Co^{3+}, and the other two fitting peaks at 781.4 and 797.9 eV belong to Co^{2+}. That matches the pure $NiCo_2O_4$. Besides, the presence of MnO_2 in the material was further confirmed by the Mn 2p signal in **Fig. 5c**. The peaks located at 642.4 eV and 653.9 eV present the Mn $2p_{3/2}$ and Mn $2p_{1/2}$ in MnO_2, respectively. Regarding the O 1s region (**Fig. 5d**), three fitting peaks are correspond to metal oxygen (M-O-M) at 529.9 eV, M-C=O at 533.0 eV, and O-C=O at 531.9 eV. All of these peaks are consistent with literatures and further testify the formation of $NiCo_2O_4$ and MnO_2.

In order to evaluate the suitability of an electrode, it is necessary to determine its the electrochemical performance in supercapacitors[52]. To evaluate the electrochemical capacitive performance of $NiCo_2O_4$@MnO_2 NNAs, CV testing was firstly performed in a three-electrode system with 6 M KOH aqueous electrolyte. **Fig. 6a** shows the CV curves of both $NiCo_2O_4$ NAs and $NiCo_2O_4$@MnO_2 NNAs at a scan rate of 5 mV s^{-1} with a voltage window ranging from -0.1 to 0.55 V (vs. Hg/HgO). Both CV curves show significant faradaic response. Two pairs of redox peaks of $NiCo_2O_4$ NAs electrode are corresponding to their reverse processes[53]. Remarkably, the $NiCo_2O_4$@MnO_2 NNAs electrode has a much larger enclosed area within the current–potential curve than that of the as-prepared $NiCo_2O_4$ NAs electrode. This is

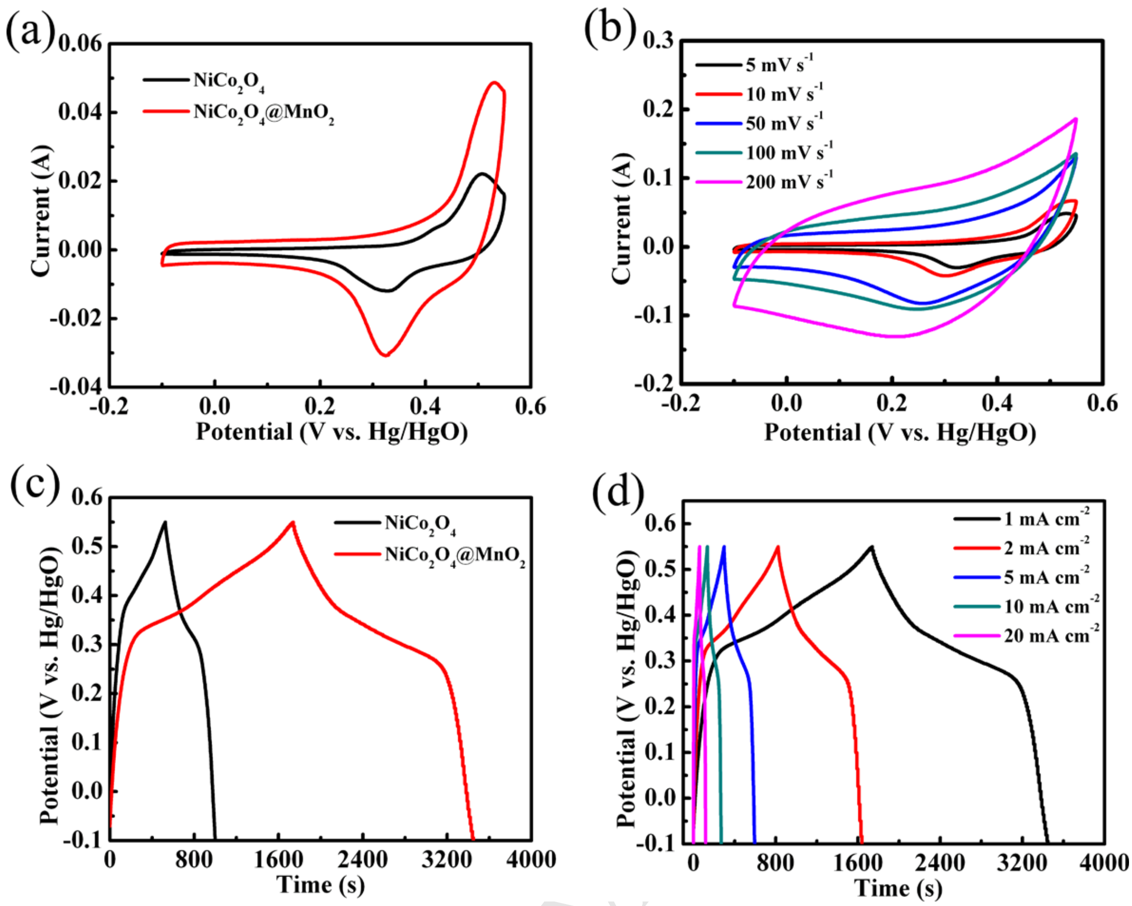

Fig. 6 CV of (a) $NiCo_2O_4$ NAs and $NiCo_2O_4$@MnO_2 NNAs at 5 mV s^{-1} and (b) $NiCo_2O_4$@MnO_2 NNAs under different scan rates in 6 M KOH; charge–discharge curves of (c) $NiCo_2O_4$ NAs and $NiCo_2O_4$@MnO_2 NNAs at 1 mA cm^{-2} and (d) $NiCo_2O_4$@MnO_2 NNAs at different current densities.

attributed to the ultrathin MnO_2 nanosheets can deliver several faradaic reactions between MnO_2/K^+, Mn^{3+}/Mn^{4+} and anion $OH^{—}$[54]. **Fig. 6b** displays typical CV curves of the $NiCo_2O_4$@MnO_2 NNAs electrode at different scan rates of 5, 10, 50, 100 and 200 mV s^{-1} with the potential of -0.1–0.55 V. From the curves, it can be seen that the CV curves retain a similar shape even at a high scan rate, implying that the hybrid electrode is favorable for fast charge-discharge process and high-rate energy storage[55]. **Fig. 6c** shows the galvanostatic charge-discharge curves of $NiCo_2O_4$ NAs and $NiCo_2O_4$@MnO_2 NNAs at 1 mA cm^{-2}, and the significantly increased discharge time of $NiCo_2O_4$@MnO_2 NNAs electrode represents its higher capacitance, which is consistent with the CV curves[56, 57]. It mainly attributes to the hierarchical core-shell structure with large specific surface area and appropriate pore distribution, which enhances redox reaction efficiency and is suitable for electrochemical energy storage. Moreover, **Fig. 6d** displays the discharge curves of the $NiCo_2O_4$@MnO_2 NNAs electrode at current densities varying from 1 to 20 mA cm^{-2}.

The areal capacitance and specific capacitance are calculated based on the discharge curves and plotted as a function of current density as shown in **Fig. 7a**. Encouragingly, the $NiCo_2O_4$@MnO_2 NNAs electrode exhibits a high areal capacitance of 5.3 F cm^{-2} at a current density of 1 mA cm^{-2}, which is much higher that of the pure $NiCo_2O_4$ NAs (1.5 F cm^{-2}). That because the large opened structure between the arrays facilitates electrolyte penetration into the inner region of the electrode, increasing the utilization of the active materials. Moreover, for the $NiCo_2O_4$@MnO_2 NNAs, the areal capacitances are calculated to be as high as 5.3, 5.0, 4.6, 4.2, and 3.6 F cm^{-2} at discharge current densities of 1, 2, 5, 10, and 20 mA cm^{-2}, respectively. Also the specific capacities are 1895.0, 1802.1, 1634.9, 1482.4, and 1303.3 F g^{-1} at the above current densities. About 68.9% of the capacitance can be retained with the current density increased 20 times, suggesting good rate performance of $NiCo_2O_4$@MnO_2 NNAs. However, just 42.2% of the capacitance retention obtained for the $NiCo_2O_4$ NAs. The ultrahigh capacitance and excellent rate performance of $NiCo_2O_4$@MnO_2 NNAs could be attributed to the combination of

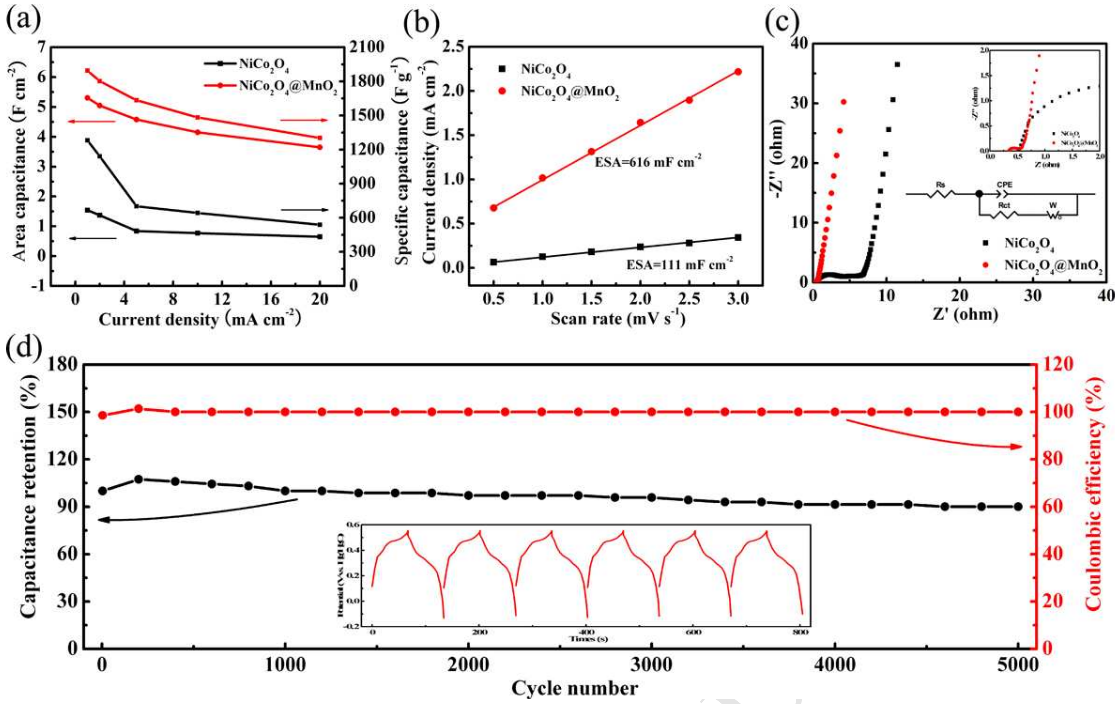

Fig. 7 (a) Areal capacitance and specific capacitance of $NiCo_2O_4$ NAs and $NiCo_2O_4@MnO_2$ NNAs at different current densities; (b) Plots of the current density at 0.285 V (vs. Hg/HgO) vs. the scan rate to determine the ESA values; (c) Nyquist plots of EIS (inset shows the enlarged area of the EIS spectra and the equivalent circuit diagram); (d) cycling performance at a constant current density of 20 mA cm^{-2}.

both the faradaic capacitance from redox reactions and EDLC on the large surface of the hierarchical structure. The EDLC contribution of $NiCo_2O_4@MnO_2$ NNAs can be measured by ESA in the non-faradaic voltage range (0.275–0.325V vs. Hg/HgO, **Fig. S3a**). The double layer charging currents are proportional to both the scan rate and the ESA of the electrode (**Fig. S3b**), which is consistent with capacitive charging behavior[58]. Thus, the ESA of $NiCo_2O_4$ NAs and $NiCo_2O_4@MnO_2$ NNAs electrode were qualitatively evaluated through the non-faradaic capacitive current upon repeated potential cycling. As shown in **Fig. 7b**, the ESA value of the $NiCo_2O_4$ NAs was just measured to be 111 mF cm^{-2}. In contrast, $NiCo_2O_4@MnO_2$ NNAs shows a much higher ESA value of 616 mF cm^{-2} (256 F g^{-1} with a mass loading of 2.4 mg cm^{-2}), which approximates to that of porous carbon (100–300 F g^{-1}). The superior ESA value verifies the enlarged active surface area and proper porosity of $NiCo_2O_4$@MnO_2 NNAs by the design of interconnected core-shell nanostructure. That also matches with the BET analysis. The enhanced electrochemical performance of the $NiCo_2O_4$@MnO_2 NNAs was further confirmed by EIS measurements as shown in **Fig. 7c**. All the curves are featured by the intersection of the curves at the real axis reveals the bulk resistance (Rs), and a semicircle in the high-frequency region which stands for the charge-transfer resistance (Rct), also a straight line in the low-frequency region which illustrates the ion diffusion resistance[59]. As observed, the $NiCo_2O_4$@MnO_2 NNAs electrode displays a very similar slope of the straight line with respect to that of the $NiCo_2O_4$ electrode, suggesting that the entire core-shell nanostructure is highly accessible for the electrolyte penetration and ion diffusion into the host materials. Besides, we can see that the $NiCo_2O_4$@MnO_2 NNAs hybrid electrode exhibits much lower charge-transfer resistance and bulk resistance than those of $NiCo_2O_4$ electrode. Because the $NiCo_2O_4$@MnO_2 NNAs hierarchical structure is with larger surface area, wide pore volume and higher pore size distribution, which endows more convenient and superb highways for the electron transport in the integrated system. Therefore, the high capacity and excellent rate capability of the $NiCo_2O_4$@MnO_2 NNAs hybrid electrode can be well explained by the distinct synergistic contribution from the $NiCo_2O_4$ core and MnO_2 shell, in which the $NiCo_2O_4$ scaffold improves the electron transport and the MnO_2 nanosheets facilitate the ion diffusion. Additionally, the cycling performance of the $NiCo_2O_4@MnO_2$ NNAs electrode is of great importance and repeated charging/discharging test over 5000 cycles at a current density of 20 mA cm^{-2} is performed, as presented in **Fig. 7d**. It is noticed that the area capability of the electrode increases at the beginning of cycling may be related to the enlarged effective interfacial area between the electrode and electrolyte along with the slow activation of the electrochemical cycling and then gradually decrease[60]. After 5000 cycles, the $NiCo_2O_4@MnO_2$ NNAs electrode delivers as high as 90.1% retention of its initial value, which suggests that the interconnected hybrid nanostructures with satisfied structural integrity is promising as electrode material for high-performance supercapacitors. Moreover, the Coulombic efficiency of the hybrid electrode is found to be nearly approaching 100%, indicating the excellent electrochemical reversibility of the electrode during the long-term cycling process. Furthermore, the EIS of the $NiCo_2O_4@MnO_2$ NNAs was measured before and after stability testing, as shown in **Fig. S4**. The EIS curve is very similar before and after the stability test, indicating that

samples	**Area specific capacitance (F cm^{-2})**	**Rate performance**	**Capacitance retention after cycling**	**Supp. Ref.**
$NiCo_2O_4@MnO_2$ nanowire arrays	3.31 (2mA cm^{-2})	50% from 2 to 20 mA cm^{-2}	88% (2000 cycles)	[48]
$Co_3O_4@NiCo_2O_4$ nanoforests	0.89 (1.6mA cm^{-2})	73% from 1.6 to 19.2 mA	157.8% (2000 cycles)	[60]

		cm^{-2}		
$NiCo_2O_4$@$NiCo_2O_4$ Nanoflakes	1.47 (5mA cm^{-2})	75% from 2 to 40 mA cm^{-2}	98.6% (4000 cycles)	[61]
CoO@MnO_2 nanosheet arrays	2.40 (2 mA cm^{-2})	40% from 2 to 64 mA cm^{-2}	——	[62]
Co_3O_4@MnO_2 nanowire arrays	0.56 (11.25 mA cm^{-2})	53% from 4 to 44.7 mA cm^{-2}	97.3% (5000 cycles)	[63]
MnO_2@NiO nanowire arrays	0.40 (5 mA cm^{-2})	55% from 5 to 25 mA cm^{-2}	96.4% (1500 cycles)	[64]
Co_3O_4@NiO nanoflakes	1.35 (6 mA cm^{-2})	——	95.1% (6000 cycles)	[23]
$NiCo_2O_4$@MnO_2 nanosheet arrays	5.30 (1 mA cm^{-2})	69% from 1 to 20 mA cm^{-2}	90.1% (5000 cycles)	This work

Table 1 Electrode properties comparison with reported literatures.

no obvious morphological defects were created in the $NiCo_2O_4$@MnO_2 NNAs. As shown in the inset of **Fig. S4**, we can see that the material still remains the $NiCo_2O_4$ nanosheet structure, but MnO_2 has some change in morphology after long-term cycling process. It maybe occured the electrochemical recrystallization process for MnO_2 owing to the repeated charge and discharge processes, which caused the surface of the material composed by some nanoparticles. Compared to previous reports, $NiCo_2O_4$@MnO_2 NNAs in our work is much superior than those of other directly-grown pseudocapacitive array nanoarchitectures, as shown in **Table 1**, such as $NiCo_2O_4@MnO_2$ nanowire arrays (3.31 F cm^{-2} at 2 mA cm^{-2})[48], $Co_3O_4@NiCo_2O_4$ nanoforests (0.89 F cm^{-2} at 1.6 mA cm^{-2})[61], $NiCo_2O_4@NiCo_2O_4$ nanoflakes (1.47 F cm^{-2} at 5 mA cm^{-2})[60] and so on. Such outstanding high electrochemical performance further proves the great advantages of the present core–shell heterostructured nanosheet arrays.

4. Conclusions

In summary, we have successfully fabricated a novel 3D $NiCo_2O_4@MnO_2$ hierarchical porous nanosheet arrays by using a facile two-step hydrothermal method. As a binder-free electrode for supercapacitors, the 3D $NiCo_2O_4@MnO_2$ NNAs reveals outstanding electrochemical properties of 5.3 F cm^{-2} at 1 mA cm^{-2}, with a capacity retention ratio of 90.1% after 5000 cycles. Such intriguing performance is attributed to the combination of both the faradaic capacitance from redox reactions and EDLC on the large surface of the hierarchical structure, which is related to unique 3D core–shell heterostructure with open geometry that providing rich active sites, also superb channels for the electrolyte penetration and ion diffusion. We believed that the hybrid $NiCo_2O_4@MnO_2$ NNAs hold great application potential for high-performance energy storage device in the future.

Acknowledgments

We are grateful for the financial support from the Natural Science Foundation of China (51674221, 51704261), the China Postdoctoral Science Foundation Funded Project (2016M591405), and Youth Scholars Research Fund of Yanshan University

(16GA012), and Science and Technology Research and Development Program of Qinhuangdao (201602A004).

References

[1] J.R. Miller, P. Simon, Electrochemical capacitors for energy management, Science 321 (2008) 651-652.

[2] F. Cai, Y. Kang, H. Chen, M. Chen, Q. Li, Hierarchical CNT@$NiCo_2O_4$ core–shell hybrid nanostructure for high-performance supercapacitors, J. Mater. Chem. A 2 (2014) 11509-11515.

[3] W. Yang, W. Yang, A. Song, G. Sun, G. Shao, 3D interconnected porous carbon nanosheet/carbon nanotube as polysulfides reservoir for high performance lithium-sulfur batteries, Nanoscale, 10 (2018) 816-824.

[4] C. Yuan, J. Li, L. Hou, X. Zhang, L. Shen, X.W.D. Lou, Ultrathin mesoporous $NiCo_2O_4$ nanosheets supported on Ni foam as advanced electrodes for supercapacitors, Adv. Funct. Mater. 22 (2012) 4592-4597.

[5] H. Xia, C. Hong, B. Li, B. Zhao, Z. Lin, M. Zheng, S.V. Savilov, S.M. Aldoshin, Facile Synthesis of Hematite Quantum-Dot/Functionalized Graphene-Sheet Composites as Advanced Anode Materials for Asymmetric Supercapacitors, Adv. Funct. Mater. 25 (2015) 627-635.

[6] X. Zheng, H. Wang, C. Wang, Z. Deng, L. Chen, Y. Li, T. Hasan, B.L. Su, 3D interconnected macro-mesoporous electrode with self-assembled NiO nanodots for high-performance supercapacitor-like Li-ion battery, Nano Energy 22 (2016) 269-277.

[7] Z. Chen, Z. Ma, J. Song, L. Wang, G. Shao, Novel one-step synthesis of

wool-ball-like Ni-carbon nanotubes composite cathodes with favorable electrocatalytic activity for hydrogen evolution reaction in alkaline solution, J. Power Sources 324 (2016) 86-96.

[8] W. Yang, W. Yang, A. Song, L. Gao, G. Sun, G. Shao, Pyrrole as a promising electrolyte additive to trap polysulfides for lithium-sulfur batteries, J. Power Sources 348 (2017) 175-182.

[9] A. Song, L. Cao, W. Yang, Y. Li, X. Qin, G. Shao, Uniform Multilayer Graphene-Coated Iron and Iron-Carbide as Oxygen Reduction Catalyst, ACS Sustainable Chem. Eng. DOI: 10.1021/acssuschemeng.7b04319.

[10] Q. Du, L. Su, L. Hou, G. Sun, M. Feng, X. Yin, Z. Ma, G. Shao, W. Gao, Rationally designed ultrathin Ni-Al layered double hydroxide and graphene heterostructure for high-performance asymmetric supercapacitor, J. Alloy. Compd. 740 (2018) 1051-1059.

[11] L. Kou, T. Huang, B. Zheng, Y. Han, X. Zhao, K. Gopalsamy, H. Sun, C. Gao, Coaxial wet-spun yarn supercapacitors for high-energy density and safe wearable electronics, Nat. commun. 5 (2014) 3754.

[12] W. Yang, W. Yang, L. Kong, A. Song, X. Qin, G. Shao, Phosphorus-doped 3D hierarchical porous carbon for high-performance supercapacitors: A balanced strategy for pore structure and chemical composition, Carbon 127 (2018) 557-567.

[13] S.W. Zhang, B.S. Yin, C. Liu, Z.B. Wang, D.M. Gu, A low-cost wearable yarn supercapacitor constructed by a highly bended polyester fiber electrode and flexible film, J. Mater. Chem. A 5 (2017), 15144-15153.

[14] B.S. Yin, S.W. Zhang, Q.Q. Ren, C. Liu, K. Ke, Z.B. Wang, Elastic soft hydrogel supercapacitor for energy storage, J. Mater. Chem. A 5 (2017), 24942-24950.

[15] M. Armand, J.-M. Tarascon, Building better batteries, Nature 451 (2008) 652-657.

[16] P.G. Bruce, B. Scrosati, J.M. Tarascon, Nanomaterials for rechargeable lithium batteries, Angew. Chem. Int. Ed. 47 (2008) 2930-2946.

[17] J.B. Goodenough, Y. Kim, Challenges for rechargeable Li batteries, Chem. Mater. 22 (2009) 587-603.

[18] J. Zhang, J. Jiang, H. Li, X. Zhao, A high-performance asymmetric supercapacitor fabricated with graphene-based electrodes, Energy Environ. Sci. 4 (2011) 4009-4015.

[19] Y. Shao, M.F. El-Kady, C.W. Lin, G. Zhu, K.L. Marsh, J.Y. Hwang, Q. Zhang, Y. Li, H. Wang, R.B. Kaner, 3D Freeze-Casting of Cellular Graphene Films for Ultrahigh-Power-Density Supercapacitors, Adv. Mater. 28 (2016) 6719-6726.

[20] W. Yang, W. Yang, F. Ding, L. Sang, Z. Ma, G. Shao, Template-free synthesis of ultrathin porous carbon shell with excellent conductivity for high-rate supercapacitors, Carbon 111 (2017) 419-427.

[21] C. Xu, B. Xu, Y. Gu, Z. Xiong, J. Sun, X. Zhao, Graphene-based electrodes for electrochemical energy storage, Energy Environ. Sci. 6 (2013) 1388-1414.

[22] M. Sun, J. Tie, G. Cheng, T. Lin, S. Peng, F. Deng, F. Ye, L. Yu, In situ growth of burl-like nickel cobalt sulfide on carbon fibers as high-performance supercapacitors, J. Mater. Chem. A 3 (2015) 1730-1736.

[23] X. Xia, J. Tu, Y. Zhang, X. Wang, C. Gu, X.-b. Zhao, H.J. Fan, High-quality metal oxide core/shell nanowire arrays on conductive substrates for electrochemical energy storage, ACS Nano, 6 (2012) 5531-5538.

[24] H. Wu, M. Xu, H. Wu, J. Xu, Y. Wang, Z. Peng, G. Zheng, Aligned NiO nanoflake arrays grown on copper as high capacity lithium-ion battery anodes, J Mater. Chem. 22 (2012) 19821-19825.

[25] L. Su, L. Gao, Q. Du, L. Hou, X. Yin, M. Feng, W. Yang, Z. Ma, G. Shao, Formation of micron-sized nickel cobalt sulfide solid spheres with high tap density for enhancing pseudocapacitive properties, ACS Sustainable Chem. Eng. 5 (2017) 9945-9954.

[26] D. Xiong, X. Li, Z. Bai, J. Li, Y. Han, D. Li, Vertically Aligned Co_9S_8 Nanotube Arrays onto Graphene Papers as High-Performance Flexible Electrodes for Supercapacitors, Chem. Eur. J. 24 (2018) 2339-2343.

[27] D. Xiong, X. Li, Z. Bai, J. Li, H. Shan, L. Fan, C. Long, D. Li, X. Lu, Rational design of hybrid Co_3O_4/graphene films: Free-standing flexible electrodes for high performance supercapacitors, Electrochim. Acta, 259 (2018) 338-347.

[28] M. Yang, X. Li, B. Yan, L. Fan, Z. Yu, D. Li, Reduced graphene oxide decorated porous SnO_2 nanotubes with enhanced sodium storage, J. Alloy. Compd. 710 (2017) 323-330.

[29] W. Liu, X. Li, D. Xiong, Y. Hao, J. Li, H. Kou, B. Yan, D. Li, S. Lu, A. Koo, K. Adair, X. Sun, Significantly improving cycling performance of cathodes in lithium ion batteries: The effect of Al_2O_3 and $LiAlO_2$ coatings on $LiNi_{0.6}Co_{0.2}Mn_{0.2}O_2$, Nano

Energy, 44 (2018) 111-120.

[30] L. Nyholm, G. Nyström, A. Mihranyan, M. Strømme, Toward flexible polymer and paper-based energy storage devices, Adv. Mater. 23 (2011) 3751-3769.

[31] G. Nyström, A. Razaq, M. Strømme, L. Nyholm, A. Mihranyan, Ultrafast all-polymer paper-based batteries, Nano Lett. 9 (2009) 3635-3639.

[32] D.P. Dubal, S.H. Lee, J.G. Kim, W.B. Kim, C.D. Lokhande, Porous polypyrrole clusters prepared by electropolymerization for a high performance supercapacitor, J. Mater. Chem. 22 (2012) 3044-3052.

[33] G. Yu, L. Hu, M. Vosgueritchian, H. Wang, X. Xie, J.R. Mcdonough, X. Cui, Y. Cui, Z. Bao, Solution-processed graphene/MnO_2 nanostructured textiles for high-performance electrochemical capacitors, Nano Lett. 11 (2011) 2905-2911.

[34] Y. He, W. Chen, X. Li, Z. Zhang, J. Fu, C. Zhao, E. Xie, Freestanding Three-Dimensional Graphene/MnO_2 Composite Networks As Ultralight and Flexible Supercapacitor Electrodes, ACS Nano, 7 (2013) 174-182.

[35] K. Qiu, Y. Lu, D. Zhang, J. Cheng, H. Yan, J. Xu, X. Liu, J.K. Kim, Y. Luo, Mesoporous, hierarchical core/shell structured $ZnCo_2O_4$ /MnO_2 nanocone forests for high-performance supercapacitors, Nano Energy, 11 (2015) 687-696.

[36] X. Liu, Y. Zhang, X. Xia, S. Shi, Y. Lu, X.L. Wang, C. Gu, J. Tu, Self-assembled porous $NiCo_2O_4$ hetero-structure array for electrochemical capacitor, J. Power Sources 239 (2013) 157-163.

[37] H. Jiang, J. Ma, C. Li, Hierarchical porous NiCo 2 O 4 nanowires for high-rate supercapacitors, Chem. Commun. 48 (2012) 4465-4467.

[38] X. Liu, S. Shi, Q. Xiong, L. Li, Y. Zhang, H. Tang, C. Gu, X. Wang, J. Tu, $NiCo_2O_4$@$NiCo_2O_4$ core/shell nanoflake arrays as high-performance supercapacitor materials. ACS Appl. Mater. Interfaces 5 (2013) 8790-8795.

[39] C. An, Y. Wang, Y. Huang, Y. Xu, C. Xu, L. Jiao, H. Yuan, Novel three-dimensional $NiCo_2O_4$ hierarchitectures: solvothermal synthesis and electrochemical properties, CrystEngComm, 16 (2014) 385-392.

[40] Y.-C. Chen, Y.-K. Hsu, Y.-G. Lin, Y.-K. Lin, Y.-Y. Horng, L.-C. Chen, K.-H. Chen, Highly flexible supercapacitors with manganese oxide nanosheet/carbon cloth electrode, Electrochim. Acta 56 (2011) 7124-7130.

[41] J.-G. Wang, Y. Yang, Z.-H. Huang, F. Kang, Coaxial carbon nanofibers/MnO_2 nanocomposites as freestanding electrodes for high-performance electrochemical capacitors, Electrochim. Acta 56 (2011) 9240-9247.

[42] D. Liu, Q. Wang, L. Qiao, F. Li, D. Wang, Z. Yang, D. He, Preparation of nano-networks of MnO_2 shell/Ni current collector core for high-performance supercapacitor electrodes, J.Mater. Chem. 22 (2012) 483-487.

[43] Q. Wang, B. Liu, X. Wang, S. Ran, L. Wang, D. Chen, G. Shen, Morphology evolution of urchin-like $NiCo_2O_4$ nanostructures and their applications as psuedocapacitors and photoelectrochemical cells, J. Mater. Chem. 22 (2012) 21647-21653.

[44] C.-C. Hu, C.-T. Hsu, K.-H. Chang, H.-Y. Hsu, Microwave-assisted hydrothermal annealing of binary Ni–Co oxy-hydroxides for asymmetric supercapacitors, J. Power Sources, 238 (2013) 180-189.

[45] M.J. Pang, S. Jiang, G.H. Long, Y. Ji, W. Han, B. Wang, X.L. Liu, Y.L. Xi, F.Z. Xu, G.D. Wei, Mesoporous $NiCo_2O_4$ nanospheres with a high specific surface area as electrode materials for high-performance supercapacitors, RSC Advances, 6 (2016), 67839-67848.

[46] M. Pang, G. Long, J. Shang, J. Yuan, H. Wei, B. Wang, X. Liu, Y. Xi, D. Wang, F. Xu, Ethanol-assisted solvothermal synthesis of porous nanostructured cobalt oxides (CoO/Co_3O_4) for high-performance supercapacitors, Chem. Eur. J. 280 (2015) 377-384.

[47] S. Jiang, M. Pang, J. Zhao, B. Xing, Q. Pan, H. Yang, W. Qu, L. Gu, H. Wang, Superior performance asymmetric supercapacitors based on a directly grown three-dimensional lawn-like cobalt-zinc hydroxyfluorides nanoneedle arrays electrode, Chem. Eur. J. 326 (2017) 1048-1057.

[48] L. Yu, G. Zhang, C. Yuan, X.W. Lou, Hierarchical $NiCo_2O_4$@MnO_2 core-shell heterostructured nanowire arrays on Ni foam as high-performance supercapacitor electrodes, Chem. Commun. 49 (2013) 137-139.

[49] Z. Ma, G. Shao, Y. Fan, G. Wang, J. Song, D. Shen, Construction of Hierarchical α-MnO2 Nanowires@ Ultrathin δ-MnO2 Nanosheets Core–Shell Nanostructure with Excellent Cycling Stability for High-Power Asymmetric Supercapacitor Electrodes, ACS Appl. Mater. Interfaces 8 (2016) 9050-9058.

[50] G. Zhang, X.W.D. Lou, General Solution Growth of Mesoporous $NiCo_2O_4$ Nanosheets on Various Conductive Substrates as High-Performance Electrodes for Supercapacitors, Adv. Mater. 25 (2013) 976-979.

[51] J. Liu, J. Jiang, C. Cheng, H. Li, J. Zhang, H. Gong, H.J. Fan, Co_3O_4 Nanowire@ MnO_2 Ultrathin Nanosheet Core/Shell Arrays: A New Class of High-Performance Pseudocapacitive Materials, Adv. Mater. 23 (2011) 2076-2081.

[52] S. Cho, M. Kim, J.S. Lee, J. Jang, Polypropylene/Polyaniline Nanofiber/Reduced Graphene Oxide Nanocomposite with Enhanced Electrical, Dielectric, and Ferroelectric Properties for a High Energy Density Capacitor, ACS Appl. Mater. Interfaces 7 (2015) 22301-22314.

[53] G.Q. Zhang, H.B. Wu, H.E. Hoster, M.B. Chan-Park, X.W.D. Lou, Single-crystalline $NiCo_2O_4$ nanoneedle arrays grown on conductive substrates as binder-free electrodes for high-performance supercapacitors, Energy Environ. Sci. 5 (2012) 9453-9456.

[54] H.-Q. Wang, G.-f. Yang, Q.-Y. Li, X.-X. Zhong, F.-P. Wang, Z.-S. Li, Y.-h. Li, Porous nano-MnO_2: large scale synthesis via a facile quick-redox procedure and application in a supercapacitor, New J. Chem. 35 (2011) 469-475.

[55] D. Kong, C. Cheng, Y. Wang, J.I. Wong, Y. Yang, H.Y. Yang, Three-dimensional Co_3O_4@C@Ni_3S_2 sandwich-structured nanoneedle arrays: towards high-performance flexible all-solid-state asymmetric supercapacitors, J. Mater. Chem. A 3 (2015) 16150-16161.

[56] D. Cai, D. Wang, B. Liu, L. Wang, Y. Liu, H. Li, Y. Wang, Q. Li, T. Wang, Three-dimensional Co_3O_4@$NiMoO_4$ core/shell nanowire arrays on Ni foam for electrochemical energy storage, ACS Appl. Mater. Interfaces 6 (2014) 5050-5055.

[57] D. Lindley, Smart grids: The energy storage problem, Nat. News 463 (2010)

18-20.

[58] G. Meng, Q. Yang, X. Wu, P. Wan, Y. Li, X. Lei, X. Sun, J. Liu, Hierarchical mesoporous NiO nanoarrays with ultrahigh capacitance for aqueous hybrid supercapacitor, Nano Energy 30 (2016) 831-839.

[59] F. Ning, M. Shao, C. Zhang, S. Xu, M. Wei, X. Duan, Co_3O_4@layered double hydroxide core/shell hierarchical nanowire arrays for enhanced supercapacitance performance, Nano Energy 7 (2014) 134-142.

[60] X. Liu, S. Shi, Q. Xiong, L. Li, Y. Zhang, H. Tang, C. Gu, X. Wang, J. Tu, Hierarchical $NiCo_2O_4$@$NiCo_2O_4$ core/shell nanoflake arrays as high-performance supercapacitor materials, ACS Appl. Mater. Interfaces 5 (2013) 8790-8795.

[61] Y. Li, Y. Zhang, Y. Li, Z. Wang, H. Fu, X. Zhang, Y. Chen, H. Zhang, X. Li, Unveiling the dynamic capacitive storage mechanism of Co_3O_4@$NiCo_2O_4$ hybrid nanoelectrodes for supercapacitor applications, Electrochimica Acta 145 (2014) 177-184.

[62] X. Wang, Y. Xiao, D. Su, S. Xu, L. Zhou, S. Wu, L. Han, S. Fang, S. Cao, Hierarchical porous cobalt monoxide nanosheet@ultrathin manganese dioxide nanosheet core-shell arrays for high-performance asymmetric supercapacitor, Int. J. Hydrogen Energy 41 (2016) 13540-13548.

[63] J. Liu, J. Jiang, C. Cheng, H. Li, J. Zhang, H. Gong, H.J. Fan, Co_3O_4 Nanowire@MnO_2 ultrathin nanosheet core/shell arrays: a new class of high-performance pseudocapacitive materials, Adv. Mater. 23 (2011) 2076-2081.

[64] J. Liu, J. Jiang, M. Bosman, H.J. Fan, Three-dimensional tubular arrays of

MnO_2–NiO nanoflakes with high areal pseudocapacitance, J. Mater. Chem. 22 (2012) 2419-2426.

Highlights:

- A cross-linked porous $NiCo_2O_4$@MnO_2 core-shell nanosheet arrays was prepared.
- Synergistic effect between two components contributes to a high area capacitance.
- The relatively high EDLC value promotes excellent rate performance.